# BiMnTeO 6 : A multiaxis Ising antiferromagnet

N. Matsubara, S. Petit, C. Martin, F. Fauth, E. Suard, S. Rols, F. Damay

# $BiMnTeO_6$ : a multi-axis Ising antiferromagnet

N. Matsubara[1,2*], S. Petit[2], C. Martin[1], F. Fauth[3], E. Suard[4], S. Rols[4], F. Damay[2]

*[1]CRISMAT, 6 bvd Maréchal Juin, 14050 Caen Cedex, France*
*[2]Laboratoire Léon Brillouin, CEA-CNRS UMR12, Université Paris-Saclay, 91191 Gif sur Yvette Cedex, France*
*[3]CELLS ALBA Synchrotron, E-08290 Barcelona, Spain*
*4 Institut Laue-Langevin, 71 avenue des Martyrs, 38042 Grenoble Cedex 9, France*

*Corresponding author: francoise.damay@cea.fr

**Version: 5 November 2019**

## ABSTRACT

The crystal and magnetic properties of honeycomb $BiMnTeO_6$ have been studied between 1.5 K and 300 K using synchrotron X-rays and neutron scattering experiments. Commensurate magnetic ordering is observed below $T_N$ = 10 K, and corresponds to a non collinear spin arrangement, with spins tilted away from the anisotropy easy-axis set by the Jahn-Teller distortion of the $MnO_6$ octahedra. Inelastic scattering experiments show two main nearly localised magnetic excitations, which can be well described by an exchange Hamiltonian involving weak Mn-Mn magnetic interactions and a crystal field Hamiltonian characterizing the strong easy-axis anisotropy associated with the $d_{z2}$ orbital ordering of $Mn^{3+}$. The crystal field levels can be accurately calculated, taking into account a transverse molecular field imposed by the magnetic ordering of the neighbouring atoms below $T_N$. This makes of $BiMnTeO_6$ an interesting example of a multi-axis Ising system in a self-imposed transverse magnetic field.

# INTRODUCTION

In the transverse Ising magnet, a magnetic field applied transverse to the spin easy-axis induces a zero Kelvin phase transition from the magnetically ordered state to a disordered, yet correlated, state [1], [2], [3], [4]. The transverse field Ising magnet (TFIM) is now the archetypal example of a system displaying a quantum phase transition [5]. Its widespread use relies on the fact that the application of a transverse field is a simple -and controllable - way to introduce quantum dynamics in an otherwise classical (Ising) system [6], [7]. It is a customary tool in many relevant topics like quantum magnetism [8], [9], or novel topological excitations [10], but also for understanding materials with unconventional properties, such as heavy fermion systems [11] and high-temperature superconductors [12]. It has been shown to successfully address anisotropic quantum phase transitions in spin chains, like for instance $LiHoF_4$ [13], [14], $BaCo_2V_2O_8$ [15] or the quantum critical point of $CoNb_2O_6$ [9], [16], while being also at the heart of more subtle phenomena governing the stability of the quantum spin ice phase in some pyrochlore materials [17], [18], [19], [20], [21], or of the intertwined polar and multipolar order on the triangular lattice magnet $TmMgGaO_4$ [22].

In this article, we show that the low energy properties of the layered honeycomb tellurate $BiMnTeO_6$ fall into TFIM physics [23]. X-ray and neutron diffraction demonstrate that this material hosts a zig-zag-like pattern of orbital orientations, resulting in $Mn^{3+}$ site-dependent magnetic easy-axes. Below $T_N$ = 10 K, those anisotropies compete with exchange interactions, to stabilize eventually a non-collinear magnetic order, out of which emerges a specific spectrum of nearly localised magnetic excitations, as observed by inelastic neutron scattering. This spectrum can be correctly modelled by considering spins with large easy-axis magnetic anisotropy, yet coupled by a molecular field arising from the ordering of

neighbouring $Mn^{3+}$ spins. This molecular field is characterized by a sizable component perpendicular (transverse) to the local easy-axis directions. Random Phase Approximation (RPA) and mean-field self-consistent calculations successfully explain both inelastic and elastic neutron scattering experiments, including the canting of the $Mn^{3+}$ spin away from the local easy-axis. *AM*$TeO_6$ layered tellurates could then prove a new way to design tunable TFIMs, playing with the nature of *A* and *M*, or with an applied external constraint like magnetic field or pressure.

## EXPERIMENTAL

*Synthesis*

$BiMnTeO_6$ was prepared by conventional solid-state reaction, starting from a mixture of $Bi_2O_3$, $Mn_2O_3$ and $H_6TeO_6$. Stoichiometric amounts of precursors were mixed in an agate mortar, before being calcined in alumina crucibles at 700°C for 24 h in $O_2$ flow. The powder was then thoroughly ground, pressed into bars (~ 2 x 2 x 12 mm) with a uniaxial press and sintered at 750°C for 12 h in $O_2$ flow.

The obtained dark brown powder of $BiMnTeO_6$ was then characterized by laboratory X-ray powder diffraction (XRPD) on a D8 ADVANCE Vario1 (Bruker) diffractometer (Cu-K$\alpha_1$ radiation) ; the monoclinic cell parameters (SG : $P2_1/c$, $a$ = 5.173 (1) Å, $b$ = 9.058 (1) Å, $c$ = 9.914 (1) Å, $\beta$ = 90.17 (1) °) used to index the diffraction pattern were found to be in excellent agreement with [23].

In-situ high-temperature XRPD measurements were also carried out using an Anton Paar HTK1200N chamber, from room temperature (RT) to 760°C in $O_2$ flow, on a flat alumina sample holder.

*Magnetic susceptibility measurements*

Magnetic measurements versus temperature were performed with a Quantum Design 5 T SQUID magnetometer, in zero-field-cooled warming (*zfcw*) and field-cooled warming (*fcw*) modes, between 5 and 300 K, in 100 Oe.

*Synchrotron X-ray and neutron diffraction*

Synchrotron X-ray powder diffraction (SXRPD) experiments were performed on the BL04-MSPD beamline at the ALBA synchrotron, at RT and 6 K with the wavelength $\lambda$ = 0.442746 and 0.442942 Å, respectively, using a rotating glass (Ø 0.3mm) capillary tube and the position sensitive detector MYTHEN. Neutron powder diffraction (NPD) was performed on the D2B (ILL, Grenoble, $\lambda$ = 1.595 Å) and G4.1 diffractometers (CEA-Saclay, France, $\lambda$ = 2.426 Å), at RT and from 1.5 to 300 K, respectively.

Symmetry analysis and Rietveld refinements were performed with tools from the FullProf Suite [24]. Symmetry analysis was carried out using the Bilbao Crystallographic Server [25], [26] and its AMPLIMODES routine [27], [28].

*Inelastic neutron scattering*

Time-of-flight (TOF) inelastic neutron scattering experiments were performed using the thermal spectrometer IN4 at the Institut Laue-Langevin (ILL, Grenoble), with two incident wavelength settings ($\lambda_i$ = 2.2 Å and 3.4 Å), at 5 K and 20 K. At 3.4 Å, the instrumental resolution is ~ 0.5 meV. Inelastic neutron scattering experiments were also performed on a cold neutron triple-axis spectrometer at LLB-Orphée (4F2, $k_f$ = 1.55 Å$^{-1}$) to study the temperature dependence of the inelastic scattering between 3 K and 50 K. Higher order contaminations were removed with a nitrogen-cooled Be filter placed in the scattered beam.

The calculations presented in the study have been carried out with the code developed in [29], [30].

## RESULTS AND DISCUSSION

### *A. Crystal structure*

The crystal structure of $BiMnTeO_6$ at RT has been refined in the monoclinic $P2_1/c$ space group (n°14), starting from the unit cell and atomic coordinates reported by Kim *et al.* [23]. This structural model provides excellent fitting to both the SXRPD and NPD data (Figure S.1a,b, S.2 and Tables S.I, S.II, S.III), and the corresponding structure is illustrated in Figure 1. $BiMnTeO_6$ can be described accordingly as a distorted honeycomb structure, closely related to trigonal $BiFeTeO_6$ or $BiCrTeO_6$ [23], [31]. This 2D crystal structure is made of edge-sharing $MnO_6$ and $TeO_6$ octahedra forming honeycomb layers in the *ab* plane, with $Bi^{3+}$ cations sandwiched between two such layers (Figure 1a). Importantly, the Mn and Te cations are fully ordered (within the refinement standard deviation), in contrast to Cr and Fe analogues [23] : the resulting topology of the Mn lattice is stacked distorted triangular planes (Figure 1b). As already stated in [23], the lower symmetry structure of $BiMnTeO_6$ (with respect to its trigonal *P*-31*c* parents) is caused by the Jahn-Teller (JT) distortion of $Mn^{3+}O_6$ octahedra, which are strongly elongated, with 4 Mn-O distances ranging between ~1.87 Å and ~1.97 Å and two Mn-O distances larger than 2.1 Å (Table S.III). On the other hand, $TeO_6$ octahedra show very little distortion, confirming its "rigid compact unit" character also reported in $Mn_2TeO_6$ [32]. The monoclinic $P2_1/c$ distortion decomposes into three distortion modes of different symmetries, corresponding to the irreducible representations (irreps) $\Gamma_1^+$,

$\Gamma_3^+$ and $M_2^-$, with isotropy subgroups *P*-31*c*, *C*2/*c* and $P2_1/c$, respectively. Their respective amplitudes show unambiguously that the larger amplitude is that of the $M_2^-$ mode (Table S.IV), thus identified as the primary order parameter. It is associated with a sheer motion of the Mn rows, triggering a rotation of the $TeO_6$ octahedra and an elongation of the $MnO_6$ ones. This is reminiscent of the structural transition observed in $Mn_2TeO_6$ [32], explained in terms of rotation of rigid $TeO_6$ units and distortion of more flexible JT active $Mn^{3+}$ octahedra. In $BiMnTeO_6$, the resulting orbital ordering pattern is a zig-zag (or herringbone) one, consisting of alternating rows with two different orbital orientations, as illustrated on Figure 1b.

The $P2_1/c$ structural model also fits the synchrotron data at 6 K (Tables S.I, S.II, S.III), showing the absence of a structural phase transition going across the magnetic ordering transition at $T_N$. Close inspection of the data of Tables S.II shows remarkably little structural change (less than 0.13%) between 300 K and 6 K, indicating that the zig-zag orbital pattern remains unchanged in that temperature range. Above RT, the monoclinic distortion of $BiMnTeO_6$ decreases discernibly with increasing temperature (Figure S.1c). At 750°C in $O_2$, just before $BiMnTeO_6$ starts to decompose, the deviation from the trigonal symmetry is slight but still visible at high Q.

### *B. Magnetic structure*

From the Curie-Weiss fitting of the paramagnetic range (see Figure S.3 and [23]), weak but clearly predominantly antiferromagnetic interactions are expected to govern the magnetic ordering of $BiMnTeO_6$. The evolution of the neutron diffraction patterns confirms this expectation, with the appearance of new Bragg peaks below $T_N$ = 10 K (Figure 2a and 2b), corroborating long-range magnetic ordering. All the magnetic Bragg peaks can be indexed with a commensurate propagation vector **k** = (½ 0 0). To constrain the number of solutions for the magnetic models, a symmetry analysis was carried out, for the Wyckoff site 4*e* of Mn.

There are four irreducible representations of dimension 1, each containing 3 basis vectors: $\Gamma_m = 3\Gamma_1 \oplus 3\Gamma_2 \oplus 3\Gamma_3 \oplus 3\Gamma_4$. The best agreement with the experimental data is obtained for the $\Gamma_1$ representation, whose basis vectors are given in Table S.V. For the single independent magnetic atom of the asymmetric unit cell, the three magnetic components $m_x$, $m_y$, and $m_z$ can be refined independently. At 1.5 K, the Rietveld refinement (Figure 2c) yields $m_x$ = 1.7(1), $m_y$ = -1.6(1) and $m_z$ = 2.8(1), which gives an ordered magnetic moment value of of 3.7(2) $\mu_B$, close to the expected value of 4 $\mu_B$ for $Mn^{3+}$ (S = 2). The resulting non-collinear magnetic structure is illustrated in Figure 2d. Its main features are antiferromagnetic chains of parallel spins running along *a*, the spin direction in two adjacent chains approximately following the zig-zag orbital pattern described earlier. This magnetic structure corresponds to the Shubnikov group $P_a2_1/c$ (#BNS 14.80), whose magnetic point group 2/*m*1' leads to zero polarization and magnetoelectric tensors.

### *C. Magnetic excitations*

From Figure 2d, one can expect magnetic exchanges to be dependent on the relative orientations of orbitals on adjacent sites: indeed, one observes collinear antiferromagnetic ordering of the spins along *a*, which would correspond to antiferromagnetic Mn-O-Te-O-Mn super-super exchange interactions [33]. Along the two other directions of the triangle, there is an alternation of up-up-down-down type configurations (although not strictly parallel), matching the alternation of short (5.093 Å) and long (5.348 Å) Mn-Mn paths. Rietveld refinement results also indicate that $Mn^{3+}$ moments are not exactly aligned along the longest axis of their octahedron, but are canted by about 20°.

To investigate these intriguing points, inelastic scattering experiments were performed. Figure 3 shows the inelastic powder spectra of $BiMnTeO_6$ mapped over momentum and energy transfer at 5 K and 20 K. Remarkably, the dominant feature of the spectrum at 5 K is

a strong almost flat band around 2 meV (Figure 3a and 3c), whose intensity decreases with increasing Q as expected for magnetic scattering. This mode seems to slightly soften and broaden for $0.6 < Q < 0.9$ Å$^{-1}$, indicating a very weak dispersion. There is no dispersive magnetic signal originating from the magnetic Bragg positions around Q = 0.6 and 0.9 Å$^{-1}$, however, as clearly seen on Figure 3c. Another weaker flat band is also observed around 3 meV. The evolution with temperature of constant Q = 0.8 Å$^{-1}$ cuts is illustrated on Figure 3d and shows clearly the existence, as high as 50 K (that is, far above $T_N$) of a magnetic signal (peaking around 1.5 meV), which evolves continuously across the magnetic transition to split into two levels at 2 and 3 meV. This behaviour strongly suggests that the magnetic spectrum is not composed of classical dispersing spin waves, but, rather, of magnetic excitons, corresponding primarily to crystal field-like levels, which are modified by an internal molecular magnetic field as spins order below $T_N$ and thus acquire a weak dispersion. They are visible in neutron scattering data provided they are characterized by $\Delta S = 1$. This scenario can be modelled using the following Hamiltonian :

$$\mathcal{H} = \mathcal{H}_{exch} + \mathcal{H}_{CEF} \qquad (1)$$

Here

$$\mathcal{H}_{exch} = \sum_{i,j} J_{ij} \mathbf{J}_i \mathbf{J}_j$$

describes the exchange interactions between spins $\mathbf{J}_i$ and $\mathbf{J}_j$ at sites $i$ and $j$, with $J_{ij}$ the exchange coupling, and

$$\mathcal{H}_{CEF} = \sum_i \left[ \sum_{l,m} B_{lm} O_{i,lm} \right]$$

describes the crystal electric field (CEF)-like Hamiltonian and characterizes the anisotropy of the 3*d* electron cloud around $Mn^{3+}$. From a general point of view, it is written in terms of the $O_{nm}$ Stevens operators [34], [35], [36], while $B_{lm}$ are the crystal field coefficients.

In the specific case of $BiMnTeO_6$, all $J_{ij}$ exchanges are considered first-neighbour. They correspond to three interactions within the triangular plane, $J_a$, $J_f$, $J_{af}$ and to an inter-plane coupling $J_C$, as drawn on Figure 1. $Mn^{3+}$ ions are located on the 4*e* site of the $P2_1/c$ structure, whose local symmetry is $C_1$. To avoid excessive over parameterization, only a single $B_{20}$ term was taken into account in the CEF Hamiltonian. Such a choice can be argued to be rather crude, considering the low symmetry of the $Mn^{3+}$ site, it is solidly warranted, however, by other examples of $Mn^{3+}$ complexes with strong JT distortion, in which the axial parameter is at least ten times the rhombic one [37], [38]. This $B_{20}$ term thus corresponds to an easy-axis anisotropy ($B_{20} < 0$), as anticipated for $Mn^{3+}$ in a JT distorted environment. Note that the main CEF *z* axis is set to *locally* correspond to the longest axis of the $MnO_6$ octahedron. It should be stressed again that this anisotropy axis changes from site to site according to the orbital pattern.

To determine the parameters of the model, the following procedure was applied. A first estimation of $B_{20}$ was assessed from the position of the broad energy level observed at 20 K (that is, when $H_{exch} = 0$, above $T_N$), at ~ 1.5 meV. This corresponds to $B_{20} = -0.17$ meV, in agreement with the expected axial magnetic anisotropy (see also Figure S.4). We then solved Eq (1) at the mean field level for each site within the magnetic unit cell:

$$\mathcal{H}_{MF} = \sum_{l,m} B_{lm} O_{i,lm} + \mathbf{J}_i \,.\, \mathbf{H}_{loc} = \sum_{l,m} B_{lm} O_{i,lm} + \mathbf{J}_i \,.\, \sum_j J_{ij} <\mathbf{J}_j>$$

$H_{loc}$ defines the molecular field experienced by a spin at site $i$. From analytical results, it is quickly inferred that the relevant parameters are $(J_a+J_C)$ and $(|J_f|+J_{af})$. A series of calculations was then performed, varying $(J_a+J_C)$ and $(|J_f|+J_{af})$. For each trial, the ground state ordered magnetic structure was determined by such self-consistent calculations. The excitonic spectrum was computed subsequently in the RPA approximation, along with the corresponding inelastic neutron cross section.

Calculations show that if ($|J_f|+J_{af}$) = 0, increasing ($J_a+J_C$) leads to a linear increase of the energy position of the four $Mn^{3+}$ crystal field levels, with only one mode being neutron active (Figure S.4). For instance, as can be seen on Figure 4a, for ($|J_f|+J_{af}$) = 0 and ($J_a+J_C$) = 0.14 meV, four energy levels are calculated, at 2.09 meV (i), 2.24 meV (ii), 3.16 meV (iii) and 3.21 meV (iv), with only (i) having a non-zero neutron cross section. It is important to underline here that, in the ($|J_f|+J_{af}$) = 0 case, the molecular field at a given site is purely longitudinal (i.e., along the local *z* axis) and proportional to ($J_a+J_C$).

A much more complex picture emerges when ($|J_f|+J_{af}$) $\neq$ 0. One example is given in Figure 4a, which illustrates the evolution of the calculated energy levels and intensities with increasing ($|J_f|+J_{af}$), for a given ($J_a+J_C$) = 0.14 meV. With increasing ($|J_f|+J_{af}$), a progressive increase of the calculated intensities of the (ii) and (iii) levels is observed, so that they become visible for ($|J_f|+J_{af}$) > 0.06 meV. Further increasing ($|J_f|+J_{af}$) leads eventually to a clear splitting of the calculated (i) and (ii) levels above ($|J_f|+J_{af}$) ~ 0.09 meV, as the energy position of the (i) level decreases, while that of the (ii) level increases. When ($|J_f|+J_{af}$) is $\neq$ 0, the molecular field is not purely longitudinal any more. Increasing ($|J_f|+J_{af}$) is equivalent to increasing the transverse components of the molecular field : this effect is shown on Figure 4b, which gives the evolution with ($|J_f|+J_{af}$) of the angle between $H_{loc}$ and the local *z* direction (as schematized on Figure 4c).

Using Figure 4a, a good modelling of the experimental data is obtained for ($|J_f|+J_{af}$) = 0.08 meV (with $B_{20}$ = -0.17 meV and ($J_a+J_C$) = 0.14 meV). The corresponding calculated powder averaged excitation spectrum, convoluted with the $Mn^{3+}$ magnetic form factor, is shown on Figure 4d, and gives excellent agreement with the experimental results of Figure 3a. A comparison between experimental and calculated Q = 0.8 $Å^{-1}$ profiles is also given on Figure 3c, to illustrate the very good match between the observed and computed positions, and relative intensities, of the two modes. The slight dispersion of the 2 meV exciton level is also

reproduced by the calculation, although it is somewhat blurred on Figure 4d, because of the powder average and the resolution function that is used to match experimental data. In the ordered spin configuration calculated as the ground state for this set of parameters, spins are tilted by 37° from their local anisotropy axis, which lies slightly above the range expected from diffraction results (Figure 4b).

## DISCUSSION

The microscopic magnetic properties of electrons in transition metal and rare-earth magnetic compounds are determined mainly by exchange and crystal field effects and their relative magnitudes. In conventional transition metal compounds, isotropic magnetic exchanges being dominant, the elementary excitations are spin waves, which are dispersive by nature. Crystal field effects appear only as small correction terms, contributing to the magnetic anisotropy.

In compounds which contain JT active cations like $Mn^{3+}$, magnetic anisotropy is imposed by the ordering of the occupied/empty electronic states (or orbital ordering) controlled by JT distortions. In extensively studied $LnMnO_3$ (Ln = La, to Gd) [39] or $TlMnO_3$ [40] perovskites, orbital ordering is not collinear, but the experimentally observed nearly collinear magnetic structures ($T_N \geq 40$ K) show that, in these compounds, Heisenberg exchange interactions are substantially larger than the energy of single ion magnetic anisotropy. The more immediate impact of orbital ordering is actually anisotropic next-nearest Heisenberg exchange interactions, which lead to in-plane ferromagnetic, but out-of-plane antiferromagnetic exchanges (so called A-structure) [41]. In contrast, in the layered triangular manganese oxide like $CuMnO_2$ [42] or $NaMnO_2$ [43], there is no competition between easy-axis anisotropy and magnetic exchanges, owing to the $d_{z2}$ ferro orbital order.

Amongst tellurates, the prominent role of orbital ordering has been emphasized recently in $Mn_2TeO_6$, through the unusually complex set of structural and magnetic transitions observed [32], [44]. The relationship between spins and orbital ordering still remains to be understood however, as both crystal and magnetic structures could be incommensurate, like in $CaMn_7O_{12}$ [45], pinpointing a delicate balance between Heisenberg exchanges and magnetic anisotropy in this compound.

On the other hand, in systems with weak magnetic exchanges and consequently low ordering temperatures (typically below 10 K), crystal fields effects are now expected to predominate : excitations correspond to local transitions between energy levels, and characterize the ground state electronic structure. Typical examples of the latter case are 4*f* compounds, and abundant literature can be found on the subject [36]. With regards to transition metals, most studies are performed on metal complexes with very weak magnetic interactions, such as molecular magnets or clusters [38], to better apprehend magnetic anisotropies or intra-clusters exchanges, and high-spin to low-spin transitions. $LaCoO_3$ in its S = 0 state is a rare example of a transition metal oxide in which neutron spectroscopic techniques have investigated the CEF energy levels [46].

$BiMnTeO_6$ is therefore a rather unusual example of a transition metal oxide, in which non collinear magnetic ordering is set by the strong easy axis anisotropy imposed by the orbital ordering. Magnetic exchange arises as a perturbation, which is quantified through the temperature evolution of the crystal field excitations at $T_N$. The choice of a single crystal field coefficient $B_{20}$ for the modelling, substantiated by the literature on $Mn^{3+}$ in JT environment, is justified *a posteriori* by the quality of the agreement between the number and energy positions of the experimental and calculated levels. In addition, the relative intensities of the 2 and 3 meV modes appearing below $T_N$, as well as the fact that there is no magnetic excitation above 4 meV on the 20 K and 5 K spectra (up to 15 meV), are very strong

constraints to the modelling, which sustain further this approximation, so that the introduction of non-diagonal terms in the $BiMnTeO_6$ CEF Hamiltonian appears unneeded at that stage.

An important outcome of this study is that it is the transverse components of the local magnetic field which are responsible for the splitting of the crystal field levels. $BiMnTeO_6$ can be therefore described as a full member of the TFIM family, whose originality resides in the zig-zag orbital pattern imposing non-collinear easy-axis anisotropies, with the transverse component of the magnetic field arising below $T_N$ only.

$BiMnTeO_6$ was recently reported as a new member of ordered $AMTeO_6$ layered honeycomb tellurates [23], [47]. Our results on $BiMnTeO_6$ underline the potential of this family as a tunable TFIM system, in which long-range exchange interactions and easy-axis anisotropy character could be adjusted, depending on the size and nature of the *A* and *M* cations. Other means, such as applied external magnetic field or pressure, could also be used to modify the ratio between the local transverse magnetic field and the easy-axis magnetic anisotropy. All these features could be used to further investigate the physics of TFIMs and the TFIM magnetic phase diagrams, to determine for instance the threshold value of the transverse field at which a quantum phase transition is observed.

## CONCLUSION

A new experimental realisation of the transverse field Ising model has been evidenced in $BiMnTeO_6$, by means of elastic and inelastic neutron scattering, combined with X-ray diffraction experiments. Magnetic ordering sets in at $T_N$ = 10 K, with no evidence of magnetoelastic effects. The magnetic ground state is made of non-collinear magnetic spins, which follow the zig-zag pattern of $d_{z2}$ orbitals existing at RT, but deviating by ~20° from their local anisotropy axis. Above $T_N$, the existence of a broad mode peaking at 1.5 meV is

attributed to a crystal field exciton. When magnetic orders sets in, this broad mode splits into two separate barely dispersive modes at ~ 2 and ~3 meV, of very distinct intensities. By means of self-consistent calculations based on a conventional Hamiltonian, using three independent parameters only, $B_{20}$ = -0.17 meV, ($J_a$+$J_C$) = 0.14 meV and ($|J_f|$+$J_{af}$) = 0.08 meV, all these experimental observations can be well reproduced. Results show in addition that the temperature dependence of the crystal field excitations originates from the increasing transverse component of the molecular field, which arises as $Mn^{3+}$ spins order.

ACKNOWLEDGEMENTS

This work was partially supported by the IUCr2017-STOE grant, awarded to Nami Matsubara, winner of the Dragons' Den contest at the IUCr2017 Congress, Hyderabad, India, 2017.

## REFERENCES


[1] R. J. ELLIOTT, P. PFEUTY, and C. WOOD, *Physical Review Letters* **25**, 443 (1970).

[2] P. PFEUTY, *Annals of Physics* **57**, 79 (1970).

[3] P. PFEUTY and R. J. ELLIOTT, *Journal of Physics Part C Solid State Physics* **4**, 2370 (1971).

[4] B. K. CHAKRABARTI, A. DUTTA, and P. SEN, editors, *Quantum Ising Phases and Transitions in Transverse Ising Models*, Springer, Berlin, 1996.

[5] S. SACHDEV, *Quantum Phase Transitions*, Cambridge University Press, Cambridge UK,, 1999.

[6] C.-J. LIN, C.-N. LIAO, and C.-H. CHERN, *Physical Review B* **85**, 134434 (2012).

[7] P. EMONTS and S. WESSEL, *Physical Review B* **98**, 174433 (2018).

[8] S. GHOSH, T. F. ROSENBAUM, G. AEPPLI, and S. N. COPPERSMITH, *Nature* **425**, 48 (2003).

[9] R. COLDEA, D. A. TENNANT, E. M. WHEELER, E. WAWRZYNSKA, D. PRABHAKARAN, M. TELLING, K. HABICHT, P. SMEIBIDL, and K. KIEFER, *Science* **327**, 177 (2010).

[10] J. ALICEA, *Reports on Progress in Physics* **75**, 076501 (2012).

[11] Q. M. SI and F. STEGLICH, *Science* **329**, 1161 (2010).

[12] S. SACHDEV, *Physica Status Solidi B-basic Solid State Physics* **247**, 537 (2010).

[13] D. BITKO, T. F. ROSENBAUM, and G. AEPPLI, *Physical Review Letters* **77**, 940 (1996).

[14] H. M. RONNOW, R. PARTHASARATHY, J. JENSEN, G. AEPPLI, T. F. ROSENBAUM, and D. F. MCMORROW, *Science* **308**, 389 (2005).

[15] Q. FAURE, S. TAKAYOSHI, S. PETIT, V. SIMONET, S. RAYMOND, L.-P. REGNAULT, M. BOEHM, J. S. WHITE, M. MANSSON, C. RUEEGG, P. LEJAY, B. CANALS, T. LORENZ, S. C. FURUYA, T. GIAMARCHI, and B. GRENIER, *Nature Physics* **14**, 716 (2018).

[16] T. LIANG, S. M. KOOHPAYEH, J. W. KRIZAN, T. M. MCQUEEN, R. J. CAVA, and N. P. ONG, *Nature Communications* **6**, 7611 (2015).

[17] J. VILLAIN, R. BIDAUX, J. P. CARTON, and R. CONTE, *Journal De Physique* **41**, 1263 (1980).

[18] R. MOESSNER, S. L. SONDHI, and P. CHANDRA, *Physical Review Letters* **84**, 4457 (2000).

[19] L. SAVARY and L. BALENTS, *Physical Review Letters* **118**, 087203 (2017).

[20] N. MARTIN, P. BONVILLE, E. LHOTEL, S. GUITTENY, A. WILDES, C. DECORSE, M. C. HATNEAN, G. BALAKRISHNAN, I. MIREBEAU, and S. PETIT, *Physical Review X* **7**, 041028 (2017).

[21] O. BENTON, *Phys. Rev. Lett.* **121**, 037203 (2018).

[22] Y. SHEN, C. L. LIU, Y. Y. QIN, S. D. SHEN, Y. D. LI, R. BEWLEY, A. SCHNEIDEWIND, G. CHEN, and J. ZHAO, *Nature Communications* **10**, 4530 (2019).

[23] S. W. KIM, Z. DENG, Z. FISCHER, S. H. LAPIDUS, P. W. STEPHENS, M. R. LI, and M. GREENBLATT, *Inorganic Chemistry* **55**, 10229 (2016).

[24] J. RODRIGUEZ-CARVAJAL, *Physica B* **192**, 55 (1993).

[25] M. I. AROYO, A. KIROV, C. CAPILLAS, J. M. PEREZ-MATO, and H. WONDRATSCHEK, *Acta Crystallographica Section A* **62**, 115 (2006).

[26] E. KROUMOVA, M. I. AROYO, J. M. PEREZ-MATO, A. KIROV, C. CAPILLAS, S. IVANTCHEV, and H. WONDRATSCHEK, *Phase Transitions* **76**, 155 (2003).

[27] J. M. PEREZ-MATO, D. OROBENGOA, and M. I. AROYO, *Acta Crystallographica Section A* **66**, 558 (2010).

[28] D. OROBENGOA, C. CAPILLAS, M. I. AROYO, and J. M. PEREZ-MATO, *Journal of Applied Crystallography* **42**, 820 (2009).

[29] S. PETIT, *Collection SFN* **12**, 105 (2011).

[30] S. PETIT, E. LHOTEL, B. CANALS, M. C. HATNEAN, J. OLLIVIER, H. MUTKA, E. RESSOUCHE, A. R. WILDES, M. R. LEES, and G. BALAKRISHNAN, *Nature Physics* **12**, 746 (2016).

[31] B. G. VATS, R. PHATAK, K. KRISHNAN, and S. KANNAN, *Materials Research Bulletin* **48**, 3117 (2013).

[32] N. MATSUBARA, F. DAMAY, B. VERTRUYEN, N. BARRIER, O. I. LEBEDEV, P. BOULLAY, E. ELKAIM, P. MANUEL, D. D. KHALYAVIN, and C. MARTIN, *Inorganic Chemistry* **56**, 9742 (2017).

[33] J. B. GOODENOUGH, *Magnetism and the Chemical Bond*, Interscience, New York, 1963.

[34] M. T. HUTCHINGS, *Solid State Physics-advances In Research and Applications* **16**, 227 (1964).

[35] A. MACKINTOSH and H. MOLLER, *Magnetic properties of rare-earth metals*, Plenum Press, 1972.

[36] B. G. WYBOURNE, *Spectroscopic Properties of Rare Earth*, John Wiley, New york, 1965.

[37] K. RIDIER, S. PETIT, B. GILLON, and G. CHABOUSSANT, *Physical Review B* **90**, 104407 (2014).

[38] R. BASLER, P. L. W. TREGENNA-PIGGOTT, H. ANDRES, C. DOBE, H. U. GUDEL, S. JANSSEN, and G. J. MCINTYRE, *Journal of the American Chemical Society* **123**, 3377 (2001).

[39] Y. TOKURA and N. NAGAOSA, *Science* **288**, 462 (2000).

[40] D. D. KHALYAVIN, P. MANUEL, W. YI, and A. A. BELIK, *Physical Review B* **94**, 134412 (2016).

[41] M. TACHIBANA, T. SHIMOYAMA, H. KAWAJI, T. ATAKE, and E. TAKAYAMA-MUROMACHI, *Physical Review B* **75**, 144425 (2007).

[42] F. DAMAY, M. POIENAR, C. MARTIN, A. MAIGNAN, J. RODRIGUEZ-CARVAJAL, G. ANDRE, and J. P. DOUMERC, *Physical Review B* **80**, 094410 (2009).

[43] M. GIOT, L. C. CHAPON, J. ANDROULAKIS, M. A. GREEN, P. G. RADAELLI, and A. LAPPAS, *Physical Review Letters* **99**, 247211 (2007).

[44] N. MATSUBARA, C. MARTIN, B. VERTRUYEN, A. MAIGNAN, F. FAUTH, P. MANUEL, V. HARDY, D. KHALYAVIN, E. ELKAIM, and F. DAMAY, *Physical Review B* **100**, 014409 (2019).

[45] N. PERKS, R. JOHNSON, C. MARTIN, L. CHAPON, and P. RADAELLI, *Nature Communications* **3**, 1277 (2012).

[46] A. PODLESNYAK, S. STREULE, J. MESOT, M. MEDARDE, E. POMJAKUSHINA, K. CONDER, A. TANAKA, M. W. HAVERKORT, and D. I. KHOMSKII, *Phys. Rev. Lett.* **97**, 247208 (2006).

[47] F. H. DING, M. L. NISBET, H. W. YU, W. G. ZHANG, L. Y. CHAI, P. S. HALASYAMANI, and K. R. POEPPELMEIER, *Inorganic Chemistry* **57**, 7950 (2018).

## FIGURE CAPTIONS

Figure 1 (color online) : $BiMnTeO_6$ structure viewed along *a* (a) and in the *ab* plane (b), showing corrugated planes separated by Bi cations, the Mn/Te order, and the $d_{z2}$ orbitals orientation (longest axis of the $MnO_6$ octahedra, shown as thick purple lines). Bi (Mn/Te/O) atoms are symbolized as yellow (purple/grey/red) spheres. Magnetic exchanges paths $J_C$, $J_{af}$, $J_f$ and $J_a$ are also shown (see text).

Figure 2 (color online) : (a) Temperature evolution of the neutron diffraction data (G4.1) between 1.5 and 12 K. (b) Corresponding temperature evolution of the Mn ordered magnetic moment (from Rietveld refinement results). The red line is a guide to the eye. (c) Rietveld refinement of the NPD pattern at 1.5 K ($R_{Bragg\ mag}$ = 7.5% and global $\chi^2$ = 3.6) (experimental data : red open circles, calculated profile : black continuous line, allowed Bragg reflections : vertical green marks ; purple marks indicate magnetic Bragg reflections. The difference between the experimental and calculated profiles is displayed at the bottom of the graph). (d) Magnetic structure of $BiMnTeO_6$ ($Mn^{3+}$ spins are shown as green arrows, longest Mn-O bonds as thick grey shapes). First-neighbor Mn-Mn distances in the triangular lattices are indicated.

Figure 3 (color online) : TOF inelastic scattering data (IN4) of $BiMnTeO_6$ at 5 K (a) and 20 K (b) (incident wavelength 3.2 Å). No additional excitation, whether of magnetic or lattice origin, are seen up to 15 meV. (c) Constant Q = 0.8 $Å^{-1}$ cut (4F2) at 3.6 K, showing the two modes at 1.8 meV and 3.1 meV. The dotted red line is calculated using Hamiltonian (1) with parameters $B_{20}$ = -0.17 meV, $(J_a+J_C)$ = 0.14 meV, $(J_{af}+|J_f|)$ = 0.08 meV. (d) Temperature evolution (up to 50 K) of constant Q = 0.8 $Å^{-1}$ cuts.

Figure 4 (color online) : (a) Calculated variation with ($J_{af}$+|$J_f$|) of the neutron cross section of $Mn^{3+}$ crystal fields transitions (($J_a$+$J_C$) = 0.14 meV, $B_{20}$ =-0.17 meV). (b) Corresponding variation with ($J_{af}$+|$J_f$|) of the angle between the anisotropy axis (axis of longest elongation of the $MnO_6$ octahedron, set parallel to *hz*) and the internal magnetic field $H_{loc}$. In (a) and (b) the green dotted line corresponds to the set of parameters giving the best agreement with the experimental data. (c) Schematic drawing of $H_{loc}$ and of its projection *hx* and *hy* (transverse components) and *hz* (longitudinal component). If $hx = hy = 0$, and $hz \neq 0$, the molecular field is purely longitudinal. (d) Calculations of the powder averaged inelastic neutron scattering excitation spectrum of $BiMnTeO_6$ (at 0 K), based on Hamiltonian (1), with parameters $B_{20}$ = -0.17 meV, ($J_a$+$J_C$) = 0.14 meV, ($J_{af}$+|$J_f$|) = 0.08 meV (calculations include the Mn magnetic form factor for direct comparison with Figure 3a).

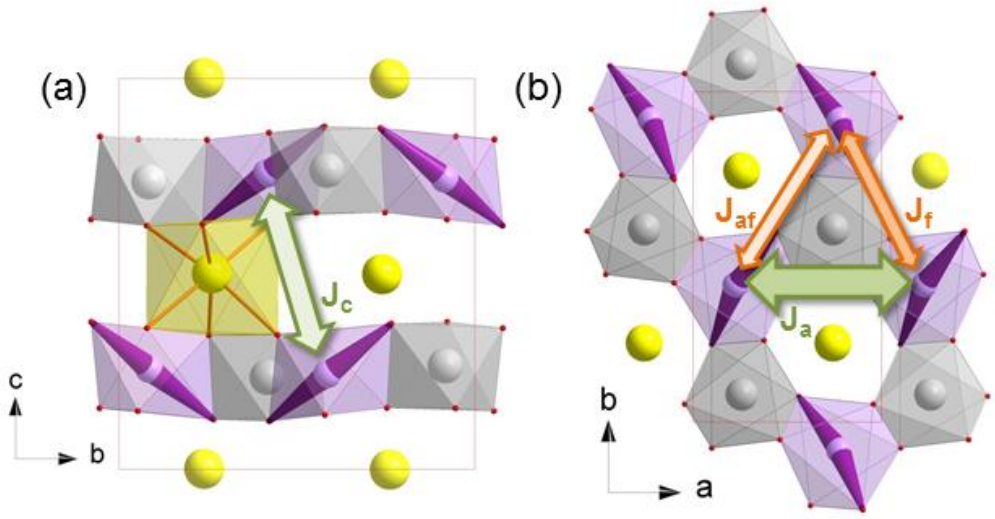


Figure 1

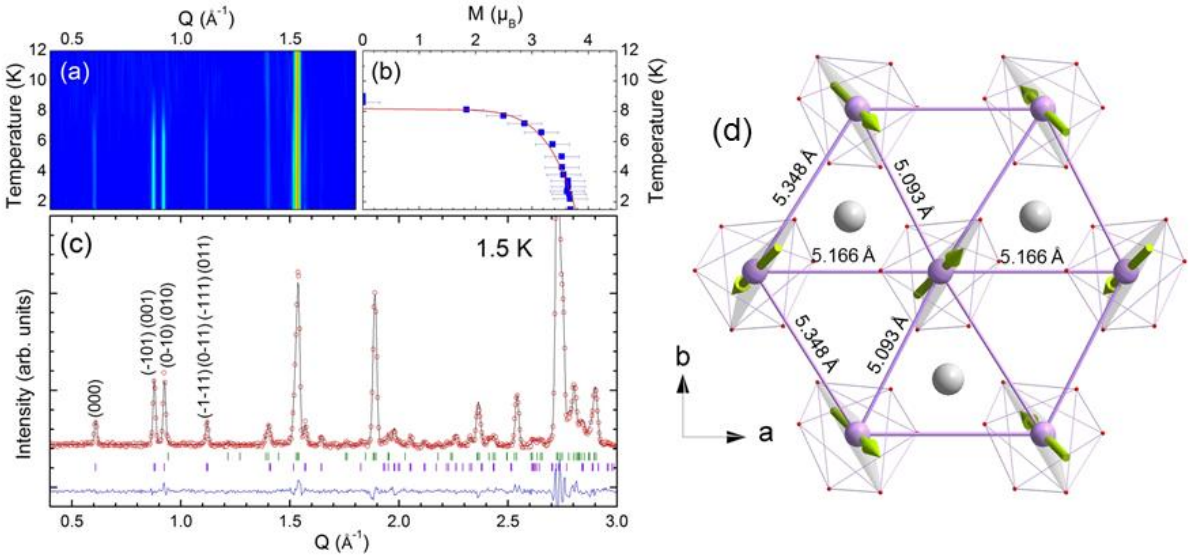


Figure 2

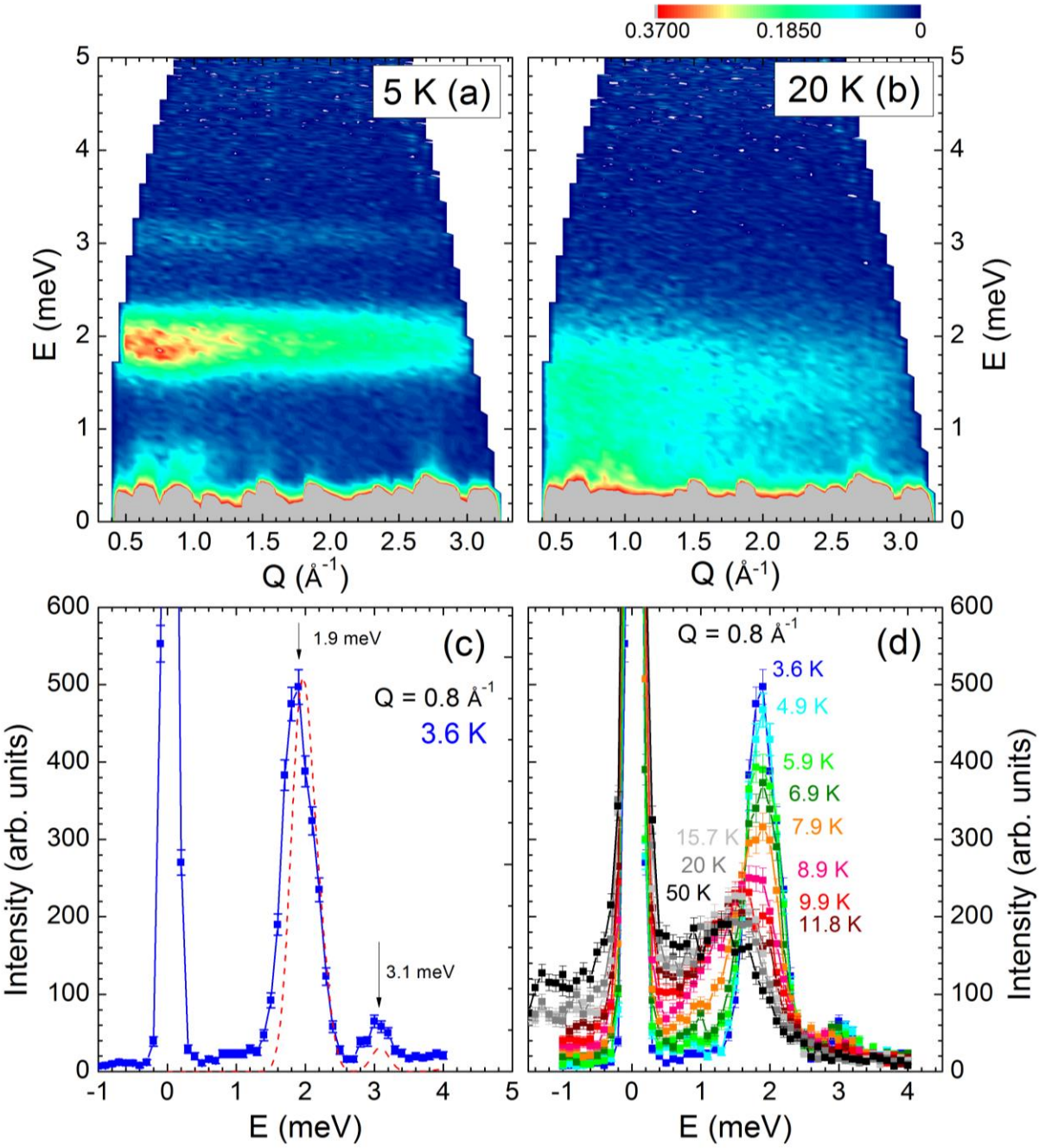
0.3700
0.1850
0
5 K (a)
20 K (b)
E (meV)
Q (Å-1)
1.9 meV
3.1 meV
(c)
Q = 0.8 Å-1
3.6 K
(d)
3.6 K
4.9 K
5.9 K
6.9 K
7.9 K
8.9 K
9.9 K
11.8 K
15.7 K
20 K
50 K
Intensity (arb. units)

Figure 3

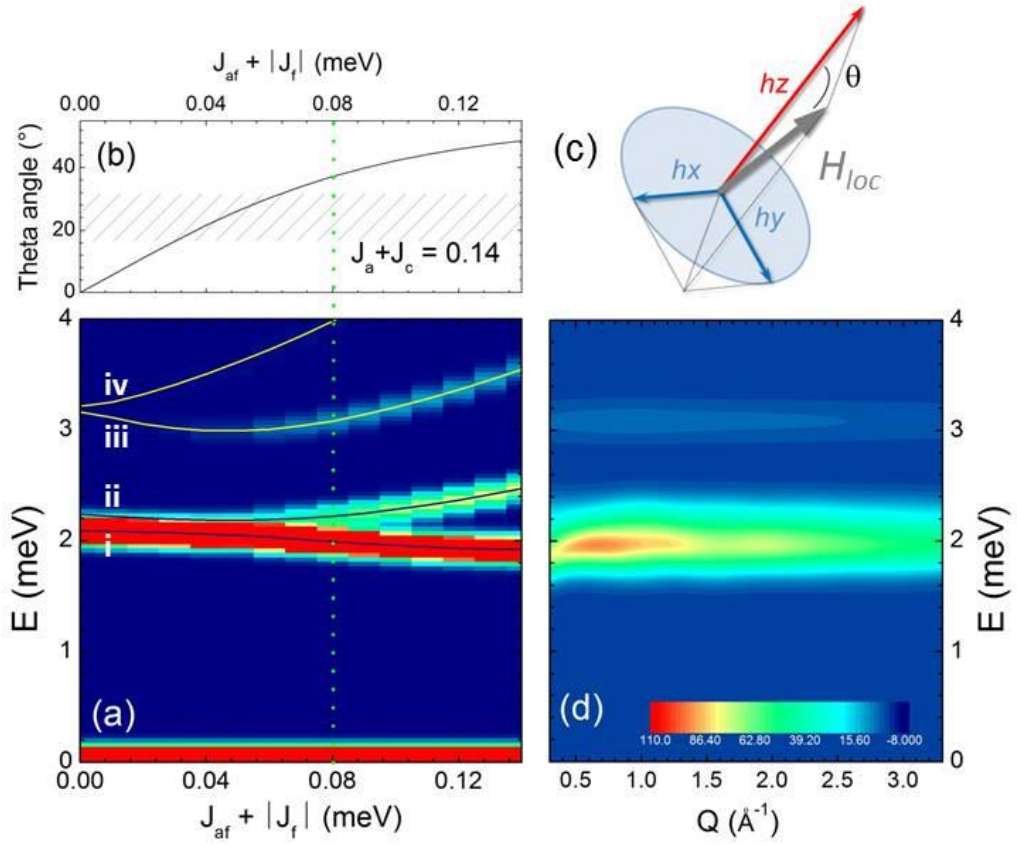
J_af + |J_f| (meV)
0.00
0.04
0.08
0.12
Theta angle (°)
(b)
J_a+J_c = 0.14
(c)
hz
θ
hx
H_loc
hy
iv
iii
ii
i
(a)
(d)
110.0
86.40
62.80
39.20
15.60
-8.000
E (meV)
Q (Å^-1)
0.5
1.0
1.5
2.0
2.5
3.0

Figure 4